



Visualization of acetaminophen-induced liver injury by time-of-flight secondary ion mass spectrometry



Yohei Murayama ^{a,*}, Shuya Satoh ^a, Akinori Hashiguchi ^b, Ken Yamazaki ^b,
Hiroyuki Hashimoto ^a, Michiie Sakamoto ^b

^a Frontier Research Center, Canon, Ohta-ku, Tokyo 146-8501, Japan

^b Department of Pathology, School of Medicine, Keio University, Shinjuku-ku, Tokyo 160-8582, Japan

ARTICLE INFO

Article history:

Received 5 November 2014

Received in revised form

24 June 2015

Accepted 9 July 2015

Available online 21 July 2015

Keywords:

Time-of-flight secondary ion MS

Imaging MS

Tissue imaging

Drug-induced liver injury

Acetaminophen

ABSTRACT

Time-of-flight secondary ion mass spectrometry (MS) provides secondary ion images that reflect distributions of substances with sub-micrometer spatial resolution. To evaluate the use of time-of-flight secondary ion MS to capture subcellular chemical changes in a tissue specimen, we visualized cellular damage showing a three-zone distribution in mouse liver tissue injured by acetaminophen overdose. First, we selected two types of ion peaks related to the hepatocyte nucleus and cytoplasm using control mouse liver. Acetaminophen-overdosed mouse liver was then classified into three areas using the time-of-flight secondary ion MS image of the two types of peaks, which roughly corresponded to established histopathological features. The ion peaks related to the cytoplasm decreased as the injury became more severe, and their origin was assumed to be mostly glycogen based on comparison with periodic acid–Schiff staining images and reference compound spectra. This indicated that the time-of-flight secondary ion MS image of the acetaminophen-overdosed mouse liver represented the chemical changes mainly corresponding to glycogen depletion on a subcellular scale. In addition, this technique also provided information on lipid species related to the injury. These results suggest that time-of-flight secondary ion MS has potential utility in histopathological applications.

© 2015 Elsevier Inc. All rights reserved.

To investigate and diagnose diseases, various staining methods have been developed to visualize the morphological and chemical information in tissue specimens. Hematoxylin and eosin (H&E)¹ staining provides useful morphological information and is the “gold standard” for pathological diagnosis. Special staining and immunohistochemical techniques offer additional information on the chemical and molecular features of specimens and can be used to extend morphological observation. During recent decades, the development of analytical techniques has enabled large amounts of chemical information to be used for this purpose. There are many promising mass spectrometry (MS) techniques, including advanced proteomics and genomics using liquid chromatography–MS [1–3], and metabolomics using gas chromatography–MS, which is now in

practical use for newborn screening [4]. Nevertheless, the difficulty in connecting chemical information and morphological information has limited the utility of MS techniques in histopathological applications. It is widely accepted that subcellular chemical changes and the subsequent morphological changes are important for evaluating disease. The proteomics, genomics, and metabolomics techniques use purified extracts of specimens that provide useful chemical information but do not provide any morphological information on their origin. For this reason, imaging mass spectrometry (IMS) [5–7] has received considerable attention. Matrix-assisted laser desorption/ionization mass spectrometry (MALDI–MS), nanoscale secondary ion mass spectrometry (nano–SIMS), and time-of-flight secondary ion mass spectrometry (TOF–SIMS) are typical IMS techniques. These techniques are classified as in situ analysis techniques that can visualize chemical information as distributions of multiple substances. MALDI–MS is considered to be suitable for the detection of large intact molecules, such as proteins and peptides, although the spatial resolution is limited to several micrometers. Of the IMS techniques, nano–SIMS has the highest spatial resolution, approaching 50 nm, although the chemical information is limited to

* Corresponding author.

E-mail address: murayama.yohei@canon.co.jp (Y. Murayama).

¹ Abbreviations used: H&E, hematoxylin and eosin; MS, mass spectrometry; IMS, imaging mass spectrometry; MALDI, matrix-assisted laser desorption/ionization; nano–SIMS, nanoscale secondary ion mass spectrometry; TOF, time-of-flight; PAS, periodic acid–Schiff; ROI, region of interest.

elemental analysis. TOF–SIMS produces secondary ion images that reflect the distribution of substances with a maximum mass of approximately 1000 at sub-micrometer spatial resolution and, therefore, has great potential for visualizing cellular and subcellular chemical information in biological samples.

Many excellent studies of single-cell imaging of cultured cells [8–18] and many approaches for visualizing the molecular distribution of tissue sections using TOF–SIMS have been reported, including for distributions of lipids in the brain [19], cholesterol ester in atherosclerotic aortic sinuses of mice [20], and specific lipids in nonalcoholic fatty liver [21]. TOF–SIMS has also been reported for subcellular visualization of tissue sections such as for visualization of cell nuclei, cell bodies and intercellular regions in mouse muscle tissue [22], and cholesterol localized in cell nuclei in rat kidney tissue [23] and brain tissue [24,25]. Furthermore, subcellular chemical changes of increased cholesterol in cell nuclei in mouse intestine tissue following cholera toxin treatment have also been visualized [19]. However, there have been few reports focused on subcellular chemical changes in individual cells in damaged tissue sections using TOF–SIMS, particularly as compared with histopathological changes.

In this study, we evaluated the use of TOF–SIMS for capturing subcellular chemical changes in damaged tissue sections. We selected mouse liver, which is a well-characterized metabolic organ, and prepared a typical acute liver injury model induced by acetaminophen overdose [26,27]. The changes on a subcellular scale were evaluated with conventional histopathological staining images. The acetaminophen-overdosed mouse liver tissue shows the following zonal features: necrotic hepatocytes in the centrilobular area, degeneration of hepatocytes in the transitional area, and nonaffected hepatocytes in the periportal area [28]. We visualized these zonal features with TOF–SIMS measurements and also evaluated the subcellular chemical changes in hepatocytes.

1. Materials and methods

1.1. Reagents

Acetaminophen, glycogen, and glucose were purchased from Sigma–Aldrich (St. Louis, MO, USA). Optimum cutting temperature compound was purchased from Sakura Fine Tek (Tokyo, Japan). Paraformaldehyde was obtained from Merck (Darmstadt, Germany). Other reagents were obtained from commercial sources.

1.2. Animals

Acetaminophen-induced liver injury model mice and control mice were prepared. All conditions were described in a previous report [13]. All animal studies were conducted in accordance with the animal experimentation guidelines of the Keio University School of Medicine.

1.3. Sample preparation

Livers harvested from mice were divided into three pieces. One piece was snap-frozen in liquid nitrogen and stored at -80°C . The remaining pieces were fixed in 10% neutral buffered formalin solution. A formalin-fixed paraffin-embedded block was prepared from one of the fixed specimens and stained with H&E and periodic acid–Schiff (PAS) stain for standard histological evaluation. The other frozen specimen was embedded in optimum cutting temperature compound and cryosectioned into $6\text{-}\mu\text{m}$ -thick sections with a cryostat (Tissue-Tek Cryo3, Sakura Fine Tek) at -20°C . These sections were then transferred onto an indium tin oxide-coated glass slide and dried in air at room temperature for TOF–SIMS

measurements. Glycogen and glucose solutions (1 mg/ml) were made with deionized water. Each solution (1 μl) was deposited onto a glass slide and dried in air at room temperature and then used to obtain the TOF–SIMS spectra of glycogen and glucose as reference compounds.

1.4. Instrumentation

TOF–SIMS spectra and images were obtained with a TOF–SIMS V instrument (ION–TOF, Münster, Germany) equipped with a Bi_n^{+} cluster primary ion gun. Positive and negative ion spectra and images were recorded using Bi_3^{+} cluster primary ions at 25 keV and electron flooding for charge neutralization. High-spatial resolution images were recorded using primary ions with a target current of 0.06 pA and a pulse width of 100 ns (high-spatial resolution mode). These images were recorded in an area covering the centrilobular zone of each section with a pixel size of approximately $1 \times 1 \mu\text{m}$. The high-mass resolution spectra were recorded using primary ions with a target current of 1.0 pA and a pulse width of 18 ns (high-mass resolution mode) for assigning and identifying the origin of the peaks. In high-mass resolution mode, the mass resolution ($m/\Delta m$, full width at half-maximum) was approximately 5000 at m/z 27. Internal mass calibration was performed using H_2^{+} , CH^{+} , CH_3^{+} , cholesterol ion ($\text{C}_{27}\text{H}_{45}^{+}$) [29], and phospholipid ion ($\text{C}_8\text{H}_{19}\text{PNO}_4^{+}$) [30] for positive ion spectra. For negative ion spectra, CH^{-} , C_2^{-} , C_2H^{-} , CHO^{-} , CH_3O^{-} , O_2^{-} , C_3H^{-} , C_4H^{-} , $\text{C}_3\text{H}_5\text{O}^{-}$, and fatty acid ion ($\text{C}_{16}\text{H}_{31}\text{O}_2^{-}$) [21] were used for precise mass calibration. Peak assignment was carried out using ion peak position, mass resolution, and mass tolerance (± 100 ppm; typical ion peaks are listed in Tables S1 and S2 of the online supplementary material) and also took into account the biological relevance obtained by pathological evaluation. In addition, many mass assignments were confirmed by comparison with reference spectra and/or the literature [21,29–35]. The images in the high-mass resolution mode were recorded with a pixel size of approximately 2×2 or $4 \times 4 \mu\text{m}$. All data were recorded with a primary ion dose density of less than 10^{13} ions cm^{-2} , which is the static SIMS limit. The data acquisition and processing were performed within Surface Lab 6 software (ION–TOF). A color scale bar, with amplitude as the number of counts, is shown on the right side of each image. The intensities of pixels were normalized to the intensity of the brightest pixel in each image. The spectra shown in each figure are the sum of all the pixels in each recorded field.

2. Results and discussion

2.1. Histology of acetaminophen-induced liver injury

Acetaminophen-overdosed mice livers and control livers were evaluated histologically by H&E and PAS staining, and centrilobular necrosis was confirmed in the acetaminophen-overdosed livers (Fig. 1). We classified the parenchyma of injured liver into the following three areas: a necrotic area devoid of glycogen, where it was difficult to distinguish individual cell borders and nuclei; a transitional area, which was distinguished by narrow bands of glycogen-depleted hepatocytes surrounding the necrotic area; and a nonaffected area. Separate parenchymal and periportal hepatocytes in nonaffected areas contained normal amounts of glycogen even in the injured liver.

2.2. Identification of nucleus and cytoplasm

First, we identified nucleus-related and cytoplasm-related ions using the TOF–SIMS spectrum and images obtained from the control mouse liver tissue. The nucleus-related ions were identified

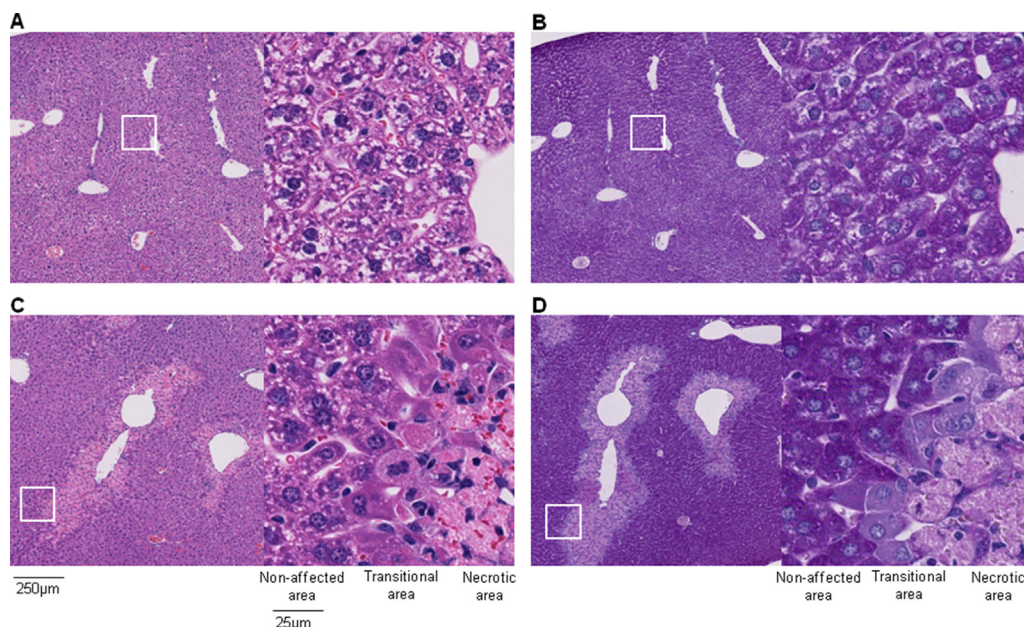


Fig. 1. Representative histological images of a liver section stained with H&E and PAS stains. Low-magnification ($5\times$, left half) and high-magnification ($40\times$, right half) images are shown. (A,B) Control mice. (C,D) Mice given an overdose of acetaminophen. (A,C) H&E staining. (B,D) PAS staining.

as CN^- and CNO^- (m/z 26 and 42, respectively), and the cytoplasm-related ions were identified as $\text{C}_x\text{H}_y\text{O}_z^-$ species such as C_2HO^- , $\text{C}_2\text{H}_3\text{O}^-$, CHO_2^- , $\text{C}_2\text{H}_3\text{O}_2^-$, and $\text{C}_3\text{H}_3\text{O}_2^-$ (m/z 41, 43, 45, 59, and 71, respectively), from images of the tissue. These ion peaks were detected with high sensitivity in the negative secondary ion spectrum (Fig. 2A). The sum images of CN^- and CNO^- and that of $\text{C}_x\text{H}_y\text{O}_z^-$ showed different patterns (Fig. 2B and C), and the overlay of the two images showed rings of $\text{C}_x\text{H}_y\text{O}_z^-$ species with diameters of 20–25 μm around $\text{CN}^- + \text{CNO}^-$ spots that were 5–10 μm in diameter (Fig. 2D). These patterns show that the $\text{C}_x\text{H}_y\text{O}_z^-$ and $\text{CN}^- + \text{CNO}^-$ ions represent the cytoplasm and nucleus in the hepatocyte, respectively.

2.3. Visualization of zonal features in injured liver tissue

We obtained the TOF–SIMS images of the tissue section of the acetaminophen-overdosed mouse liver by using the $\text{CN}^- + \text{CNO}^-$ and $\text{C}_x\text{H}_y\text{O}_z^-$ ions detected in the negative ion spectrum (Fig. 3A–C). The image showed zonal features and could be classified into the following three areas (Fig. 3C): a necrotic area, where both signal distributions had no shape and were weak; a transitional area, where the bright $\text{CN}^- + \text{CNO}^-$ signals formed dot structures surrounded by dark $\text{C}_x\text{H}_y\text{O}_z^-$ signals; and a nonaffected area, which had bright $\text{CN}^- + \text{CNO}^-$ signals that formed dot structures surrounded by bright $\text{C}_x\text{H}_y\text{O}_z^-$ signals. These zonal

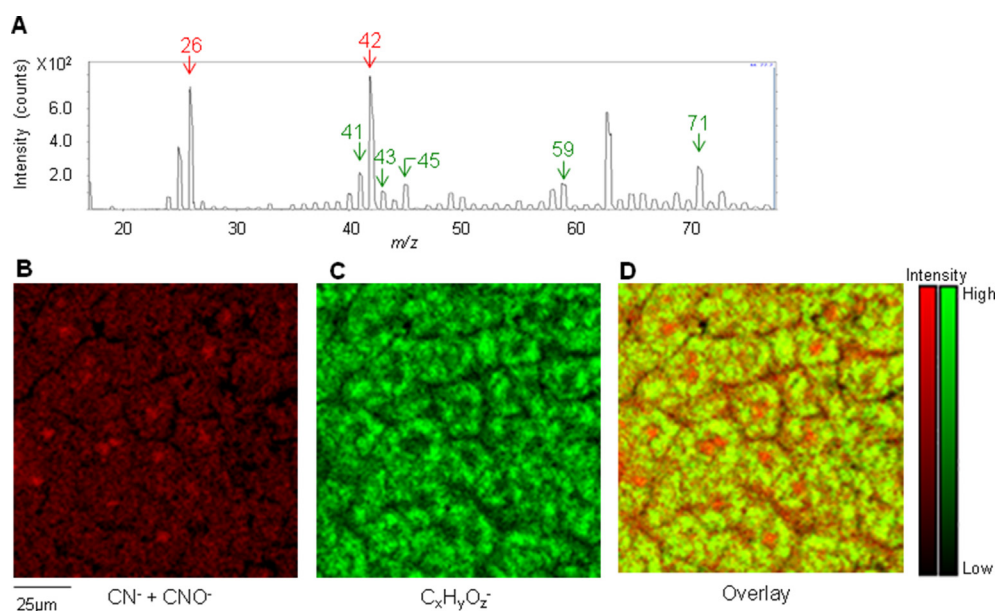


Fig. 2. Negative ion spectrum and images obtained from control mouse liver by TOF–SIMS in high-spatial resolution mode. (A) Spectrum. (B) Sum image of $\text{CN}^- + \text{CNO}^-$ (m/z 26 and 42). (C) Sum image of $\text{C}_x\text{H}_y\text{O}_z^-$ (m/z 41, 43, 45, 59, and 71). (D) Overlay image of panels B and C. $\text{CN}^- + \text{CNO}^-$ is shown in red, and $\text{C}_x\text{H}_y\text{O}_z^-$ is shown in green.

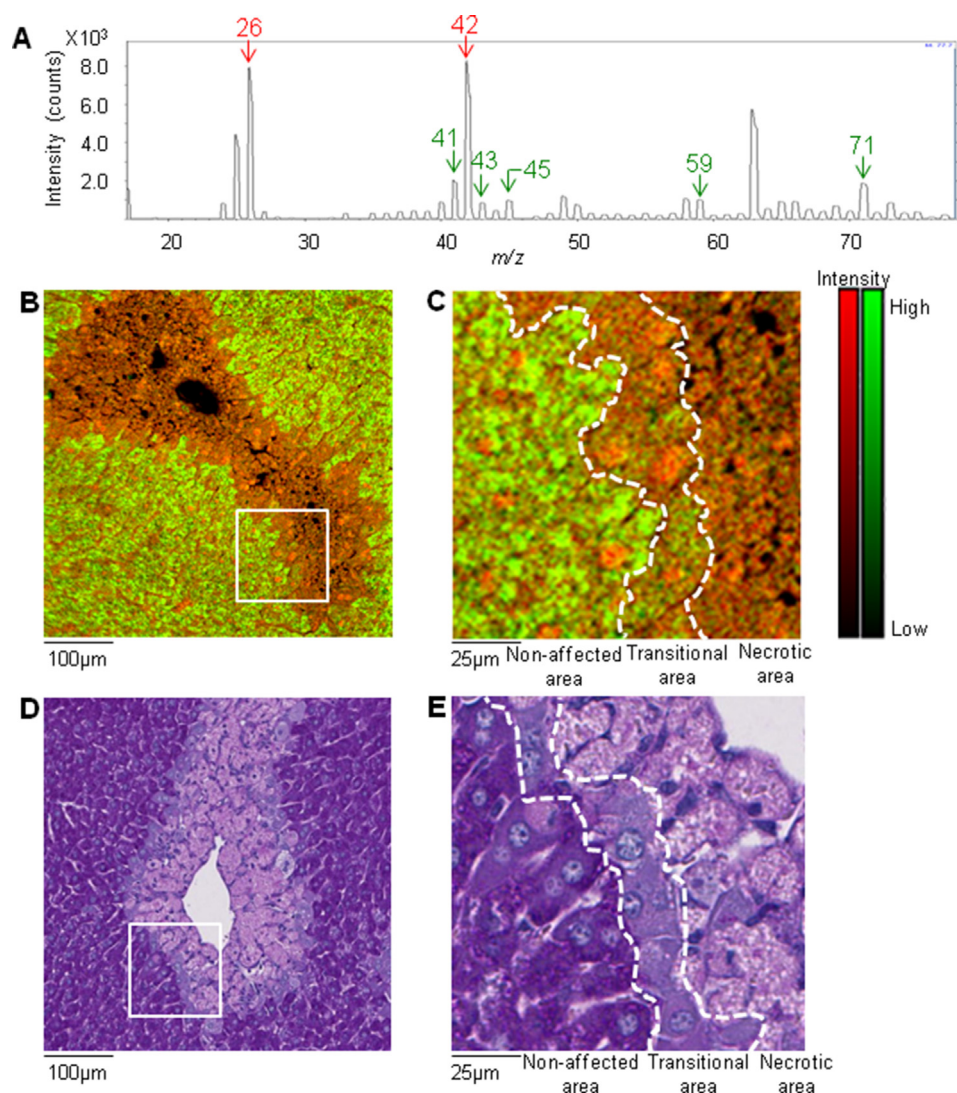


Fig. 3. Negative ion spectrum and images obtained from acetaminophen-overdosed mouse liver by TOF–SIMS in high-spatial resolution mode. (A) Spectrum. (B) Overlay images of $\text{CN}^- + \text{CNO}^-$ (m/z 26 and 42) and $\text{C}_x\text{H}_y\text{O}_z^-$ (m/z 41, 43, 45, 59, and 71). $\text{CN}^- + \text{CNO}^-$ is shown in red, and $\text{C}_x\text{H}_y\text{O}_z^-$ is shown in green. (C) Magnifications of the areas in the white squares in panel B. (D) PAS staining images obtained from adjacent formalin-fixed paraffin-embedded section (the same section is shown in Fig. 1D). (E) Magnifications of the areas in the white squares in panel D. Panels B to E include the three areas of liver tissue. The dotted white lines in panels C and E indicate the boundaries between areas.

features in the TOF–SIMS image roughly corresponded to those in the PAS staining image shown in Fig. 3D and E.

The zonal features in the TOF–SIMS image were semi-quantitatively evaluated. We selected the entire region of each of the three areas shown in Fig. 3C as regions of interests (ROIs). The changes in the signal intensity of the $\text{CN}^- + \text{CNO}^-$ and $\text{C}_x\text{H}_y\text{O}_z^-$ ions in the three areas are summarized in Fig. 4. The signal intensities of the $\text{CN}^- + \text{CNO}^-$ and $\text{C}_x\text{H}_y\text{O}_z^-$ ions in each area were counted and averaged by the total number of pixels in each area. The averaged intensities per pixel in the necrotic area and the transitional area were normalized to those in the nonaffected area. The ROI analysis showed that the signal intensity of $\text{CN}^- + \text{CNO}^-$ decreased in only the necrotic area, whereas that of $\text{C}_x\text{H}_y\text{O}_z^-$ decreased gradually with the progression of the injury. These changes in signal intensity corresponded approximately to the results obtained by PAS staining.

Here, the charging effect and the so-called matrix effect, normally present in TOF–SIMS analysis, should be carefully considered for quantitative evaluation. Our experimental results on these two

effects are as follows. First, it is well known that an accumulation of static charge on the sample surface decreases detection sensitivity [36] and that the accumulation level differs not only from sample to sample but also from measurement to measurement within the same sample. In our experiment, the influence of charging effect was minimized by electron flooding and the use of data from the same field of view in the same tissue section. However, total ion images (shown in Fig. S1 of the supplementary material) suggested that the localized charging effect existed at the left edge of a field of view of $500 \times 500 \mu\text{m}$ under our measurement conditions. To avoid this region, all ROIs were extracted from a small area of less than $150 \times 150 \mu\text{m}$ at the right side of the measured field (Fig. 3B and C). Therefore, we thought that the charging effect was roughly uniform across the ROIs. Another result obtained from a different region in the same tissue under the same measurement conditions, including the sample tilt, supported the above-mentioned influence of the charging effect, as noted in Figs. S2 and S3 of the supplementary material. As shown in these figures, a similar charging effect was observed in the field of view of $500 \times 500 \mu\text{m}$, and similar changes

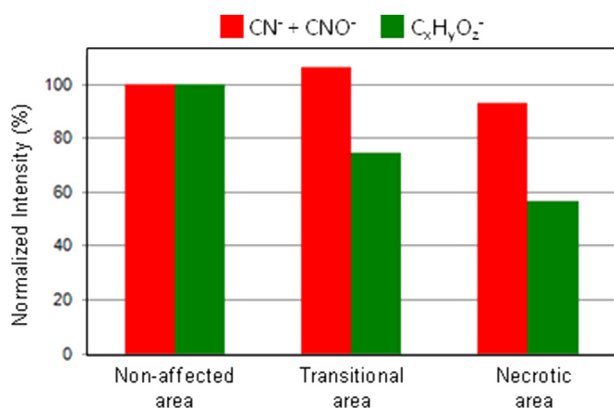


Fig. 4. Evaluation of the change in signal intensity in the TOF–SIMS image of acetaminophen-overdosed mouse liver shown in Fig. 3C. The signal intensity was extracted from three ROIs, which were the three areas shown in Fig. 3C. The intensities of the CN⁻ + CNO⁻ and C_xH_yO_z⁻ peaks are the values averaged by the total number of pixels in each area and normalized by the averaged intensity in the nonaffected area. CN⁻ + CNO⁻ is shown in red, and C_xH_yO_z⁻ is shown in green.

were observed in signal intensity in the three areas. Second, the matrix effect is also known to affect the signal intensities by chemical microenvironment of a compound [37]. In the negative ion mode, halogen and phosphate ions are expected to influence the signal intensity for a biological tissue sample. However, the halogen and phosphate ions did not show characteristic distributions corresponding to the three zonal features in our experiments, demonstrating that the matrix effect was roughly uniform across the three areas. Thus, our assessment is that neither the charging effect nor the matrix effect caused the changes in signal intensity shown in Fig. 4.

To interpret the chemical information in the TOF–SIMS image shown in Fig. 3, we investigated the origins of the CN⁻, CNO⁻, and C_xH_yO_z⁻ ions. The CN⁻ and CNO⁻ ions from the tissue sections were reported previously as fragment ions for proteins and nucleotides contained in cell nuclei in tissue sections [32], and there are various sources of CN⁻ and CNO⁻ ions. In general, this variety causes the observed changes of their signal intensity. In this study, cellular autophagy and karyolysis, which are associated with the loss of proteins and nucleotides, were remarkable in the injured liver tissues, as shown in Fig. 1. Therefore, the interpretation that proteins and nucleotides were the possible sources of the CN⁻ and CNO⁻ ions in our data is consistent with the decrease of these peaks in the necrotic area shown in Fig. 4. There have also been reports that HeLa cells give C_xH_yO_z⁻ ions [14] and that the source of the ions in carbohydrate microarrays is saccharide [38]. In this study, we assumed that the C_xH_yO_z⁻ ions originated mainly from glycogen by comparing TOF–SIMS and PAS staining images, which visualize the distribution of glycogen (shown in Fig. 3) and the high concentration of glycogen usually contained in the liver. This assignment was almost consistent with the additional analysis using purified glycogen as described below. The section of the reference spectra for the high-mass resolution measurement of glycogen is shown in Fig. 5A (the full spectrum is shown in Fig. S4A of the supplementary material). For comparison, spectra obtained from the tissue sections of the control and acetaminophen-overdosed mice livers in the same mode are shown in Fig. 5C and D. The tissue section and the measured field of view of the acetaminophen-overdosed mice liver in this mode were the same as those in the high-spatial resolution mode. As shown in Fig. 5E, it was confirmed that the image of the C_xH_yO_z⁻ peaks in Fig. 5D had contrast similar to that shown in green in Fig. 3B. The glycogen film

exhibited a C_xH_yO_z⁻ peak pattern similar to that of the tissue sections, as shown in Fig. 5A. Glucose, which is the monomer of glycogen and is also abundant in the liver, also produced a C_xH_yO_z⁻ peak pattern, as shown in Fig. 5B (the full spectrum is shown in Fig. S4B of the supplementary material).

We then marked the glycogen fragment ion peak at *m/z* 221.1 as a more specific peak because its molecular weight is higher than that of glucose and the signal intensity from glucose was quite low (Fig. 5A and B). Broad ion peaks at *m/z* 221.1 (detailed information is given in Figs. S4A and S4C and Table S3 in the supplementary material) were detected from mice liver tissues (Fig. 5C and D). The broadness of these peaks may have been caused by the coexistence of multiple ion species within a narrow mass range, making the assignment difficult in general. However, the ion peak at *m/z* 221.1, as well as the C_xH_yO_z⁻ peaks, was detected mainly from the non-affected area where glycogen was dominant (Fig. 5E and G). This suggested that glycogen was the major source of the ion peaks at *m/z* 221.1 and could contribute to the production of the C_xH_yO_z⁻ peaks, at least in the tissue sections used for our study. In contrast, our data could not clarify the influence of glucose on the C_xH_yO_z⁻ peaks because of the low peak specificity and the poor contrast in the images of the other ions of glucose, such as deprotonated ion ([M–H]⁻) at *m/z* 179.1, in tissue sections (Fig. 5C, D and F). TOF–SIMS analysis cannot detect intact glycogen owing to its very high molecular weight of approximately 100,000; therefore, further experiments would be necessary to identify the C_xH_yO_z⁻ peaks exactly. However, the comparison with PAS staining and reference spectra of glycogen indicated that the C_xH_yO_z⁻ ions mainly give responses for glycogen.

The above results indicated that the TOF–SIMS image (Fig. 3B and C) represented chemical changes mainly corresponding to glycogen depletion on a subcellular scale. In general, diseased tissues consist of cells in different phases. The difference reflects chemical changes over time. We can use the difference to understand the history of disease progression. In pathology, glycogen metabolism is an important chemical change that can be visualized by PAS staining. Our results show the potential of TOF–SIMS to recognize this kind of difference through observing the distribution of subcellular and cellular changes.

2.4. Analysis of injury-related lipids

TOF–SIMS also provided information about alteration of lipids. A positive secondary ion spectrum obtained from the tissue section of the acetaminophen-injured mouse liver in the high-spatial resolution mode is shown in Fig. 6A. The fragment ion peaks of cholesterol were detected at *m/z* 95, 109, 147, and 369, and those of phospholipids were also detected at *m/z* 86, 104, 166, 184, and 206. These peaks were assigned by use of the high-mass resolution spectrum (Fig. S5 and Table S1 in supplementary material) and by comparison with previously published studies that investigated fragment ions of various lipids [30,33,34]. The overlay image of cholesterol (*m/z* 109 and 369) and phospholipids (*m/z* 184), which were detected as single peaks in the case of high-mass resolution mode, is shown in Fig. 6B. Phospholipids were dominant in the necrotic area, whereas cholesterol was not.

To obtain more information on the species of phospholipids that were dominant in the necrotic area, TOF–SIMS analysis was performed on the same tissue section in high-mass resolution mode. The positive and negative secondary ion spectra are shown in Fig. 7A and B (the full spectra are shown in Figs. S5 and S6 of the supplementary material). The phospholipid ion peaks were detected (exact masses are listed in Tables S1 and S2 of the supplementary material). In the positive ion spectrum, the precursor ions of diacyl phosphatidylcholine 32:0 were detected at *m/z* 734.6

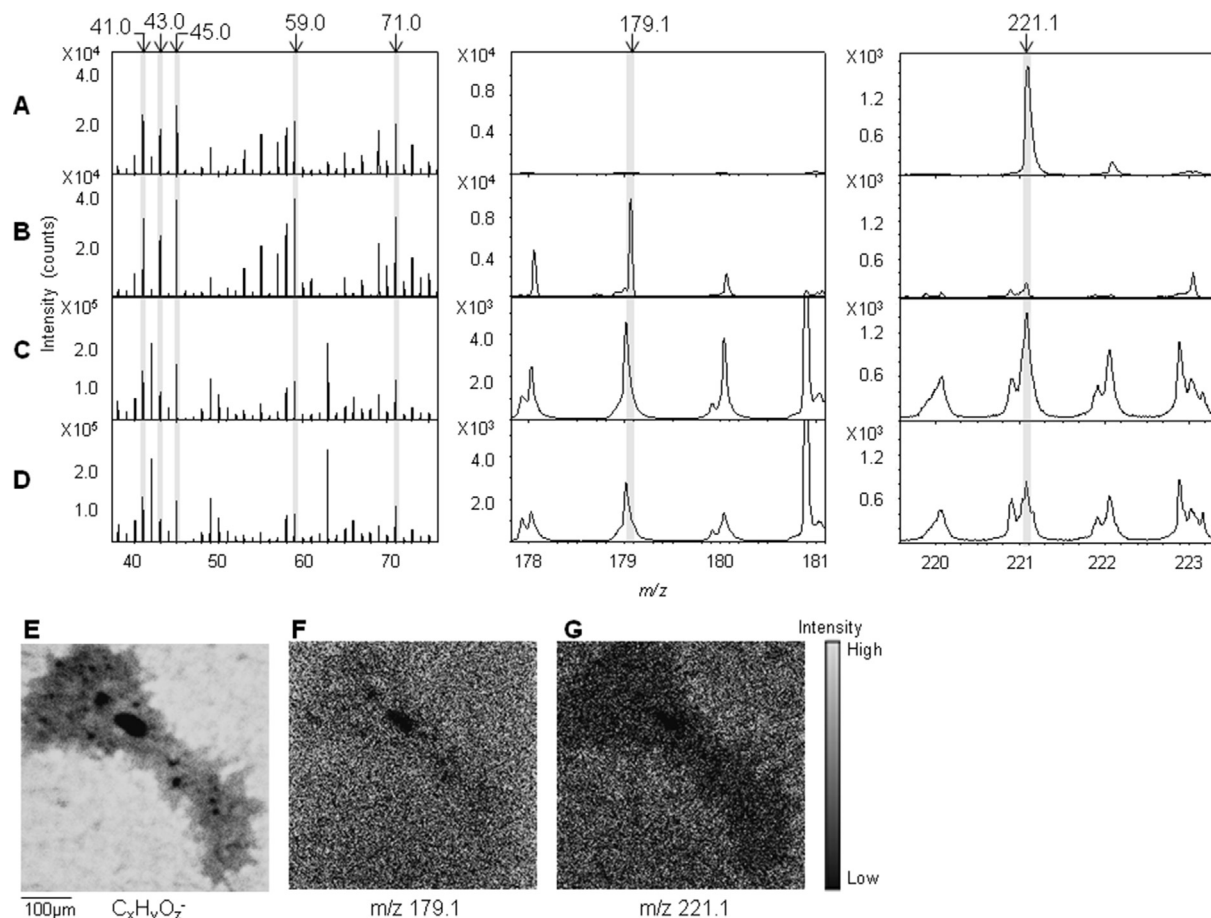


Fig. 5. Spectra of reference compounds and liver tissue sections and images of $C_xH_yO_z^-$, m/z 179.1 (deprotonated glucose ion), and m/z 221.1 (glycogen fragment ion) obtained from acetaminophen-overdosed mouse liver by TOF-SIMS in high-mass resolution mode. (A–D) Negative ion spectra obtained from glycogen film (A), glucose film (B), control mouse liver (C), and acetaminophen-overdosed mouse liver (D). (E–G) Images obtained from acetaminophen-overdosed mouse liver reconstructed from $C_xH_yO_z^-$ (m/z 41, 43, 45, 59, and 71) (E), m/z 179.1 (deprotonated glucose ion) (F), and m/z 221.1 (glycogen fragment ion) (G).

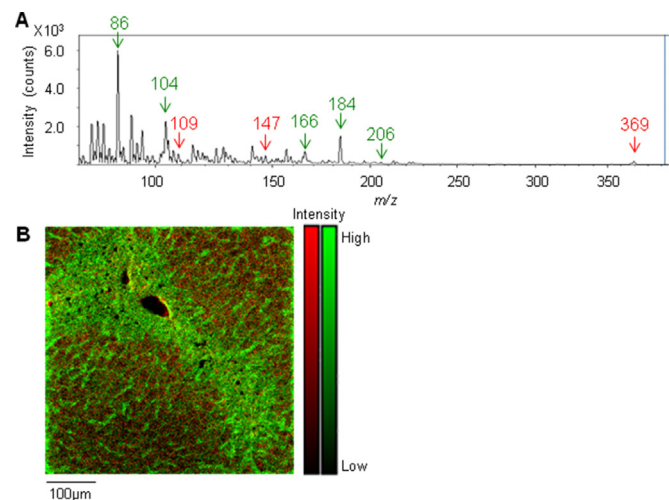


Fig. 6. Positive ion spectrum and image obtained from acetaminophen-overdosed mouse liver by TOF-SIMS in high-spatial resolution mode. (A) Spectrum. (B) Overlay image of cholesterol (m/z 109 and 369, shown in red) and phospholipids (m/z 184, shown in green).

($[M+H]^+$) and 772.5 ($[M+K]^+$), and those of diacyl phosphatidylcholine 34:1 were also detected at m/z 760.6 ($[M+H]^+$) and m/z 798.5 ($[M+K]^+$). In the negative ion spectrum, the fragment ions of sphingomyelin 34:1 were detected at m/z 642.5 ($[M-N(CH_3)_3]^-$) and 687.5 ($[M-CH_3]^-$). These assignments were performed by exact mass, mass tolerance (Tables S1 and S2), and comparison with the literature [21,31,32,35]. The images of each molecular species are shown in Fig. 7C–E. Diacyl phosphatidylcholine 32:0 and sphingomyelin 34:1 were increased in the necrotic area, whereas diacyl phosphatidylcholine 34:1 was not. Phosphatidylcholine and sphingomyelin, which are major cell membrane components, may be related to the breakdown of the cell membrane by cell death. The behavior of these lipids in injured tissue was beyond the scope of this study; however, it was shown that the molecular structures of lipids, such as the number of carbon chains and double bonds, could be related to the injury.

Information on lipid species cannot be obtained by conventional staining methods. In formalin-fixed paraffin-embedded sections, the morphology of lipids can be indirectly visualized as defects formed by elution of lipids during delipidation. In fresh frozen sections, fat staining can directly visualize lipids but cannot provide information on their chemical composition. Therefore, the information on lipid species is hardly used in routine histopathological evaluation. In contrast, in metabolomics and lipidomics, which use MS techniques, various lipid species have been identified and

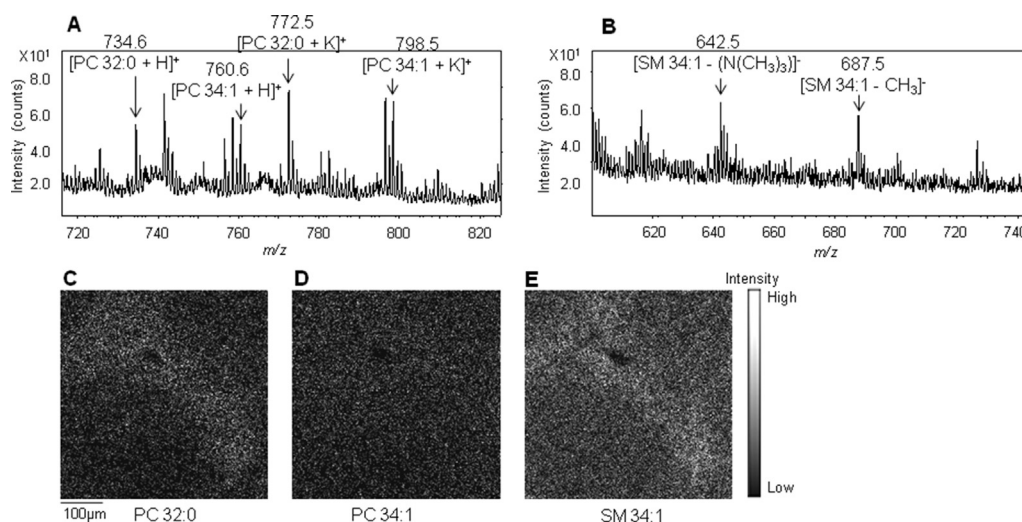


Fig. 7. Positive and negative ion spectra and images obtained from acetaminophen-overdosed mouse liver by TOF-SIMS in high-mass resolution mode. (A) Positive ion spectrum. (B) Negative ion spectrum. (C) Image of diacyl phosphatidylcholine 32:0 (PC 32:0) (m/z 734.6 and 772.5). (D) Image of diacyl phosphatidylcholine 34:1 (PC 34:1) (m/z 760.6 and 798.5). (E) Image of sphingomyelin 34:1 (SM 34:1) (m/z 642.5 and 687.5).

researched as biomarker candidates [39–43]. TOF-SIMS, which can provide the information on lipid species and their distributions, could be a powerful tool for using lipid information as an additional index in histopathological research.

2.5. Future applications and problems in TOF-SIMS

We have demonstrated that TOF-SIMS can capture subcellular chemical changes and show the altered distribution of injury-related substances, such as glycogen and lipids, in acetaminophen-induced liver injury. This indicates the potential utility of the technique in histopathological analysis. Furthermore, the compatibility of the high-spatial resolution and molecular specificity used in this study reveals the advantage of TOF-SIMS for other IMS techniques. However, there are still technical problems to be solved before TOF-SIMS can be used for practical applications in histopathology. The detection sensitivity for high-mass peaks ($m/z > 1000$) is still too low. The high-mass peaks can provide much information about the molecular species in biological tissues. To improve the sensitivity, gas cluster ions have been used for TOF-SIMS. It has been reported that using gas cluster ions as the primary ions provided large secondary ions that were undetectable with conventional TOF-SIMS using metal ions [44–47]. In addition, the low throughput for TOF-SIMS measurements is also a problem. The typical measurement time in TOF-SIMS is several tens of minutes with a field of view of $500 \times 500 \mu\text{m}$ and a pixel size of approximately $1 \times 1 \mu\text{m}$. This time is too long compared with that for optical microscope imaging. Improving the detection sensitivity may resolve this issue, although other approaches, such as the use of stigmatic TOF-SIMS, should also be considered.

3. Conclusion

In this study, the alteration of cellular substances in acetaminophen-overdosed mouse liver tissue was visualized by TOF-SIMS. The TOF-SIMS image using ion peaks related to the nucleus and cytoplasm in the hepatocyte successfully classified three areas in acetaminophen-overdosed mouse liver roughly corresponding to established histopathological features. The ion peaks related to the cytoplasm decreased with progression of the injury, and their origin was assumed to be mostly glycogen based on comparison with

the PAS staining image and the spectra of reference compounds. This indicated that the TOF-SIMS image represented chemical changes mainly corresponding to glycogen depletion on a subcellular scale. In addition, TOF-SIMS provided the information on the lipid species related to the injury. Further studies are needed to further demonstrate the utility of TOF-SIMS in histopathological applications.

Acknowledgments

This study was supported by a research grant from Canon. The authors thank J. Naito and M. Tsukamoto for providing technical assistance with TOF-SIMS measurements.

Appendix A. Supplementary material

Supplementary material related to this article can be found at <http://dx.doi.org/10.1016/j.ab.2015.07.005>.

References

- [1] D.A. Megger, T. Bracht, H.E. Meyer, B. Sitek, Label-free quantification in clinical proteomics, *Biochim. Biophys. Acta* 1834 (2013) 1581–1590.
- [2] X. Han, A. Aslanian, J.R. Yates III, Mass spectrometry for proteomics, *Curr. Opin. Chem. Biol.* 21 (2008) 483–490.
- [3] D. Globish, M. Münzel, M. Müller, S. Michalakakis, M. Wagner, S. Koch, T. Brückl, M. Biel, T. Carell, Tissue distribution of 5-hydroxymethylcytosine and search for active demethylation intermediates, *PLoS One* 5 (2010) e15367.
- [4] T. Kuhara, Diagnosis of inborn errors of metabolism using filter paper urine, urease treatment, isotope dilution, and gas chromatography–mass spectrometry, *J. Chromatogr. B* 758 (2001) 3–25.
- [5] P. Chaurand, S.A. Schwartz, R.M. Caprioli, Imaging mass spectrometry: a new tool to investigate the spatial organization of peptides and proteins in mammalian tissue sections, *Curr. Opin. Chem. Biol.* 6 (2002) 676–681.
- [6] E.R.A. van Hove, D.F. Smith, R.M.A. Heeren, A concise review of mass spectrometry imaging, *J. Chromatogr. A* 1217 (2010) 3946–3954.
- [7] D. Touboul, O. Laprévote, A. Brunelle, Micrometric molecular histology of lipids by mass spectrometry imaging, *Curr. Opin. Chem. Biol.* 15 (2011) 725–732.
- [8] D. Breitenstein, C.E. Rommel, R. Möllers, J. Wegener, B. Hagenhoff, The chemical composition of animal cells and their intracellular compartments reconstructed from 3D mass spectrometry, *Angew. Chem. Int. Ed.* 46 (2007) 5332–5335.
- [9] P.D. Piehowski, A.M. Davey, M.E. Kurczyk, E.D. Sheets, N. Winograd, A.G. Ewing, M.L. Heien, Time-of-flight secondary ion mass spectrometry imaging of subcellular lipid heterogeneity: Poisson counting and spatial resolution, *Anal. Chem.* 81 (2009) 5593–5602.
- [10] J.S. Fletcher, S. Rabbani, A. Henderson, N.P. Lockyer, J.C. Vickerman, Three-dimensional mass spectral imaging of HeLa-M cells: sample preparation, data

- interpretation, and visualization, *Rapid Commun. Mass Spectrom.* 25 (2011) 925–932.
- [11] J.S. Fletcher, J.C. Vickerman, N. Winograd, Label free biochemical 2D and 3D imaging using secondary ion mass spectrometry, *Curr. Opin. Chem. Biol.* 15 (2011) 733–740.
- [12] M.K. Passarelli, A.G. Ewing, N. Winograd, Single-cell lipidomics: characterizing and imaging lipids on the surface of individual *Aplysia californica* neurons with cluster secondary ion mass spectrometry, *Anal. Chem.* 85 (2013) 2231–2238.
- [13] E.B. Monroe, J.C. Jurchen, J. Lee, S.S. Rubakhin, J.V. Sweedler, Vitamin E imaging and localization in the neuronal membrane, *J. Am. Chem. Soc.* 127 (2005) 12152–12153.
- [14] J. Brison, M.A. Robinson, D.S.W. Benoit, S. Muramoto, P.S. Stayton, D.G. Castner, TOF–SIMS 3D imaging of native and non-native species within HeLa cells, *Anal. Chem.* 85 (2013) 10869–10877.
- [15] S.A. Parry, M.E. Kurczyk, X. Fan, M.S. Halleck, R.A. Schlegel, N. Winograd, Imaging macrophages in trehalose with SIMS, *Appl. Surf. Sci.* 255 (2008) 929–933.
- [16] S.G. Ostrowski, C.T. Van Bell, N. Winograd, A.G. Ewing, Mass spectrometric imaging of highly curved membranes during *Tetrahymena* mating, *Science* 305 (2004) 71–73.
- [17] C.A. Barnes, J. Brison, M. Robinson, D.J. Graham, D.G. Castner, B.D. Ratner, Identifying individual cell types in heterogeneous cultures using secondary ion mass spectrometry imaging with C_{60} etching and multivariate analysis, *Anal. Chem.* 84 (2012) 893–900.
- [18] S.G. Ostrowski, M.E. Kurczyk, T.P. Roddy, N. Winograd, A.G. Ewing, Secondary ion MS imaging to relatively quantify cholesterol in the membranes of individual cells from differentially treated populations, *Anal. Chem.* 79 (2007) 3554–3560.
- [19] K. Börner, P. Malmberg, J. Månsson, H. Nygren, Molecular imaging of lipids in cells and tissues, *Int. J. Mass Spectrom.* 260 (2007) 128–136.
- [20] E. Lee, H.K. Shon, T.G. Lee, S. Kim, D.W. Moon, The regional ratio of cholesteryl palmitate to cholesteryl oleate measured by ToF–SIMS as a key parameter of atherosclerosis, *Atherosclerosis* 226 (2013) 378–384.
- [21] D. Debois, M. Bralet, F.L. Naour, A. Brunelle, O. Laprévotte, In situ lipidomic analysis of nonalcoholic fatty liver by cluster TOF–SIMS imaging, *Anal. Chem.* 81 (2009) 2823–2831.
- [22] D.J. Graham, D.G. Castner, Image and spectral processing for ToF–SIMS analysis of biological materials, *Mass Spectrom. (Tokyo)* 2 (2014) S0014.
- [23] H. Nygren, P. Malmberg, C. Kriegeskotte, H.F. Arlinghaus, Bioimaging TOF–SIMS: localization of cholesterol in rat kidney sections, *FEBS Lett.* 566 (2004) 291–293.
- [24] H. Nygren, K. Börner, B. Hagenhoff, P. Malmberg, J. Månsson, Localization of cholesterol, phosphocholine, and galactosylceramide in rat cerebellar cortex with imaging TOF–SIMS equipped with a bismuth cluster ion source, *Biochim. Biophys. Acta* 1737 (2005) 102–110.
- [25] H. Nygren, K. Börner, P. Malmberg, B. Hagenhoff, Localization of cholesterol in rat cerebellum with imaging TOF–SIMS effect of tissue preparation, *Appl. Surf. Sci.* 252 (2006) 6975–6981.
- [26] J.L. Raucy, J.M. Lasker, C.S. Lieber, M. Black, Acetaminophen activation by human liver cytochromes P450IIE1 and P450IA2, *Arch. Biochem. Biophys.* 271 (1989) 270–283.
- [27] J.A. Hinson, D.W. Roberts, L.P. James, Mechanisms of acetaminophen-induced liver necrosis, *Handb. Exp. Pharmacol.* 196 (2010) 369–405.
- [28] S. Satoh, Y. Otsuka, Y. Ozeki, K. Itoh, A. Hashiguchi, K. Yamazaki, H. Hashimoto, M. Sakamoto, Label-free visualization of acetaminophen-induced liver injury by high-speed stimulated Raman scattering spectral microscopy and multivariate image analysis, *Pathol. Int.* 64 (2014) 518–526.
- [29] A.G. Sostarecz, C.M. McQuaw, A.G. Ewing, N. Winograd, Phosphatidylethanolamine-induced cholesterol domains chemically identified with mass spectrometric imaging, *J. Am. Chem. Soc.* 126 (2004) 13882–13883.
- [30] H. Yang, I. Ishizaki, N. Sanada, N. Zaima, Y. Sugiura, I. Yao, K. Ikegami, M. Setou, Detection of characteristic distributions of phospholipid head groups and fatty acids on neurite surface by time-of-flight secondary ion mass spectrometry, *Med. Mol. Morphol.* 43 (2010) 158–164.
- [31] M.K. Passarelli, N. Winograd, Lipid imaging with time-of-flight secondary ion mass spectrometry (ToF–SIMS), *Biochim. Biophys. Acta* 1811 (2011) 976–990.
- [32] P. Sjövall, B. Johansson, J. Lausmaa, Localization of lipids in freeze-dried mouse brain sections by imaging TOF–SIMS, *Appl. Surf. Sci.* 252 (2006) 6966–6974.
- [33] P.D. Piehowski, A.J. Carado, M.E. Kurczyk, S.G. Ostrowski, M.L. Heien, N. Winograd, A.G. Ewing, MS/MS methodology to improve subcellular mapping of cholesterol using TOF–SIMS, *Anal. Chem.* 80 (2008) 8662–8667.
- [34] I. Lanekoff, M.E. Kurczyk, R. Hill, J.S. Fletcher, J.C. Vickerman, N. Winograd, P. Sjövall, A.G. Ewing, Time of flight mass spectrometry imaging of samples fractured in situ with a spring-loaded trap system, *Anal. Chem.* 82 (2010) 6652–6659.
- [35] P. Sjövall, J. Lausmaa, B. Johansson, Mass spectrometric imaging of lipids in brain tissue, *Anal. Chem.* 76 (2004) 4271–4278.
- [36] K.H. Kim, Z. Akase, T. Suzuki, D. Shindo, Charging effects on SEM/SIM contrast of metal/insulator system in various metallic coating conditions, *Mater. Trans.* 51 (2010) 1080–1083.
- [37] E.A. Jones, N.P. Lockyer, J.C. Vickerman, Mass spectral analysis and imaging of tissue by ToF–SIMS: The role of buckminsterfullerene, C_{60} , primary ions, *Int. J. Mass Spectrom.* 260 (2007) 146–157.
- [38] D.J. Scurr, T. Horlacher, M.A. Oberli, D.B. Werz, L. Kroeck, S. Bufali, P.H. Seeberger, A.G. Shard, M.R. Alexander, Surface characterization of carbohydrate microarrays, *Langmuir* 26 (2010) 17143–17155.
- [39] C. Hu, R. van der Heijden, M. Wang, J. van der Greef, T. Hankemeier, G. Xu, Analytical strategies in lipidomics and applications in disease biomarker discovery, *J. Chromatogr. B* 877 (2009) 2836–2846.
- [40] H. Ogiso, T. Suzuki, R. Taguchi, Development of a reverse-phase liquid chromatography electrospray ionization mass spectrometry method for lipidomics, improving detection of phosphatidic acid and phosphatidylserine, *Anal. Biochem.* 375 (2008) 124–131.
- [41] M. Arita, Mediator lipidomics in acute inflammation and resolution, *J. Biochem.* 152 (2012) 313–319.
- [42] D.L. Gorden, P.T. Ivanova, D.S. Myers, J.O. McIntyre, M.N. VanSaun, J.K. Wright, L.M. Matrisian, H.A. Brown, Increased diacylglycerols characterize hepatic lipid changes in progression of human NAFLD comparison to a murine model, *PLoS One* 6 (2011) e22775.
- [43] M. Kawashima, N. Iwamoto, N. Kawaguchi-Sakita, M. Sugimoto, T. Ueno, Y. Mikami, K. Terasawa, T. Sato, K. Tanaka, K. Shimizu, M. Toi, High-resolution imaging mass spectrometry reveals detailed spatial distribution of phosphatidylinositols in human breast cancer, *Cancer Sci.* 104 (2013) 1372–1379.
- [44] K. Mochiji, M. Hashinokuchi, K. Moritani, N. Toyoda, Matrix-free detection of intact ions from proteins in argon-cluster secondary ion mass spectrometry, *Rapid Commun. Mass Spectrom.* 23 (2009) 648–652.
- [45] S. Aoyagi, J.S. Fletcher, S. Sheraz (Rabbani), T. Kawashima, I.B. Razo, A. Henderson, N.P. Lockyer, J.C. Vickerman, Peptide structural analysis using continuous Ar cluster and C_{60} ion beams, *Anal. Bioanal. Chem.* 405 (2013) 6621–6628.
- [46] J. Matsuo, S. Torii, K. Yamauchi, K. Wakamoto, M. Kusakari, S. Nakagawa, M. Fuji, T. Aoki, T. Seki, Novel SIMS system with focused massive cluster ion source for mass imaging spectrometry with lateral resolution, *Appl. Phys. Express* 7 (2014) 056602.
- [47] H. Gnaser, M. Fujii, S. Nakagawa, T. Seki, T. Aoki, J. Matsuo, Prolific cluster emission in sputtering of phenylalanine by argon-cluster ion bombardment, *Int. J. Mass Spectrom.* 360 (2014) 54–57.